Synthesis, Structural Analysis, and Degradation Behaviour of Potassium Tin Chloride as Chloride-Ion Batteries Conversion Electrode Material

Soutam Panja[1]*, Yidong Miao[1], Johannes Döhn[3], Jaehoon Choi[1], Simon Fleischmann[1], Shivaraju Guddehalli Chandrappa[1], Thomas Diemant[1], Axel Groß[1,3], Guruprakash Karkera[1]*, Maximilian Fichtner[1,2]*

1 Helmholtz Institute Ulm for Electrochemical Energy Storage (HIU), 89081 Ulm, Germany
2 Institute of Nanotechnology, Karlsruhe Institute of Technology (KIT), 76021 Karlsruhe, Germany
3 Institute of Theoretical Chemistry, Ulm University, 89081 Ulm, Germany

E-Mail: m.fichtner@kit.edu; karkera.guruprakash@uni-ulm.de; soutam.panja@uni-ulm.de

Abstract

Chloride ion batteries (CIBs) offer a compelling alternative to lithium-ion systems, particularly in applications demanding cost-effectiveness and resource sustainability. However, the development of tailored electrode materials remains a critical bottleneck for CIB advancement. In this study, we synthesized an untapped class of perovskite-based material potassium hexachlorostannate (K_2SnCl_6, denoted as KSC) via a facile mechanochemical route for the first time. The prepared KSC was subjected to various characterization techniques to confirm its crystal structure and morphology. Herein, KSC exhibited intriguing electrochemical performance in a non-aqueous CIB configuration, utilizing a lithium metal counter electrode. Furthermore, *ex-situ* X-ray diffraction (XRD) and X-ray photoelectron spectroscopy (XPS) analysis, reveal a conversion reaction mechanism involving chloride ion shuttling and provide insights into structural evolution during cycling. Moreover, the Density functional theory (DFT) studies supported additional degradation products that could potentially limit the performance of these materials, limiting the performance of these materials as potential battery electrodes in CIBs.

1. Introduction

Lithium-ion batteries (LIBs) have become the dominant power source for portable electronics and automotive applications.[1] The depletion of lithium resources worldwide necessitates the exploration of alternative electroactive species that can be extracted from cheap and abundant raw materials to establish a sustainable and economically viable new chain in energy storage. Therefore, there has been a growing interest in post-Li batteries based on Na^+, K^+, Ca^{2+}, and Zn^{2+} cation shuttles as viable alternatives to LIBs.[2,3] However, developing alternative battery systems with long cycle life and low cost, without sacrificing energy density, remains a challenge. Recently, there has been growing interest in rechargeable batteries based on an anion shuttle, such as chloride or fluoride batteries that operate at room temperature.[4] CIBs show significant potential as future power sources due to their high theoretical energy density (~2500 Wh L^{-1}).[5] Despite their larger ionic radius compared to Li^+, Mg^+, O^{2-} and F^-, Cl^- ions offer higher ionic mobility in the electrolyte, which could lead to faster reaction kinetics. A typical CIB is composed of a metal chloride electrode that supplies chloride ions, an electrolyte for

1

carrying the Cl⁻ ions, and a counter electrode with a low reduction potential.[6] In literature, several materials have been studied at the cathode side, however, stability issues arising from the dissolution of these materials in the applied organic electrolytes were often encountered, which precluded their application in chloride ion batteries.[7,8] The development of a stable electrode material, which exhibits lower volume expansion than existing metal chlorides, remains an unresolved challenge. Metal oxychlorides[8] such as FeOCl, BiOCl, and VOCl have recently been explored as cathode materials, offering improved electrochemical performance and stability over metal chloride-based cathodes. Furthermore, $Sb_4O_5Cl_2$ [9] and a $Sb_4O_5Cl_2$/graphene aerogel composite ($Sb_4O_5Cl_2$-GAG)[10] were employed as anodes for aqueous CIBs and cathodes for non-aqueous CIBs, respectively. The ability of metal oxychlorides to function effectively as active material in both anodes and cathodes, depending on the working conditions, underscores their adaptability in CIB technology.

Perovskites with a chemical formula of ABX_3 possess valuable properties for batteries and supercapacitors,[11] which has led to their use as electrodes and electrolytes. As an example, the promising potential of perovskite halides like $CsSnCl_3$[12] and $CsSn_{0.9}In_{0.067}Cl_3$[13] as chloride ion conductors were demonstrated. Despite this, there is a surprising lack of exploration into their specific application as electrodes within CIBs. This highlights the clear need for focused research into developing novel perovskite-based electrodes specifically designed for CIBs. In this study, we investigate KSC, as a new electrode material for non-aqueous chloride ion batteries. K_2SnCl_6 materials are synthesized by a one-pot mechanochemical ball-milling route which is, in comparison to high-temperature sintering techniques and organic solvent-assisted processes, a more effective way.[14–16] The electrochemical performance of the anti-fluorite structured K_2SnCl_6 is investigated in non-aqueous electrolytes with lithium metal as anode. Furthermore, to understand the structural changes during cycling and the electrochemical reaction mechanism, ex-situ XRD and XPS measurements are conducted. The experimental insights were complemented by theoretical investigations within the framework of periodic density functional theory (DFT) where potential pathways for the electrode reaction were examined and based on a theoretical stability analysis a number of potential decomposition reactions were derived.

2

2. Results and Discussion

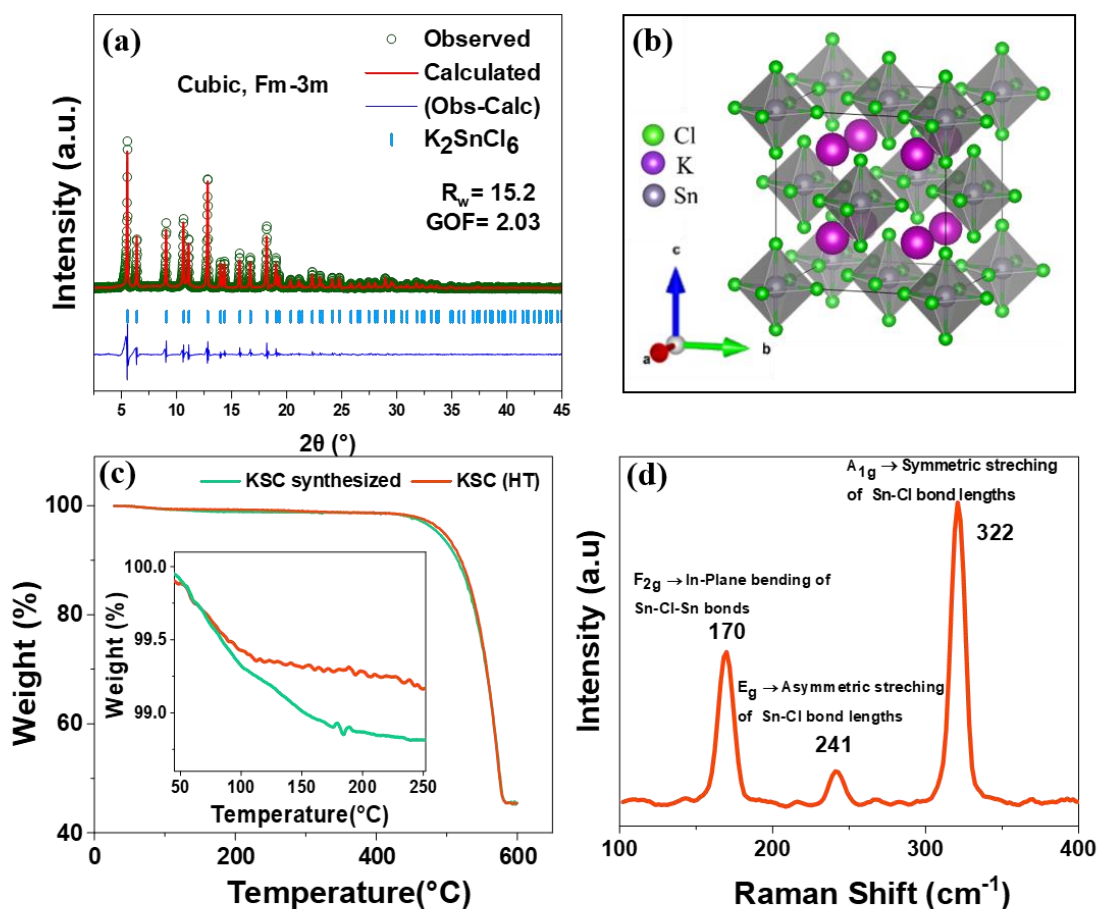### 2.1. Characterization of pristine KSC

Figure 1. (a) XRD data of pristine KSC (dried) including Rietveld refinement, (b) crystal structure of KSC with Cl (green), K (purple), and Sn (grey) atoms (c) TGA curves of as synthesized ("KSC synthesized") and dried sample ("KSC (HT)") and (d) Raman spectrum of KSC (dried).

The refined XRD pattern and crystal structure of as-synthesized KSC (dried) are displayed in **Figures 1a and 1b** respectively.[17] Rietveld refinement of the KSC powder diffraction data using GSAS II revealed a cubic unit cell with space group *Fm-3m* (#225-1). The lattice parameters were refined to be a = b = c = 10.01390 Å with all angles $\alpha = \beta = \gamma = 90°$. The unit cell volume was determined to be 1004.1757 Å^3. A thermogravimetric analysis (TGA) curve was used to compare the weight loss of the as-synthesized and dried samples, the results are shown in **Figure 1c**. These measurements confirmed the removal of small amounts of residual water in the temperature range between 50 and 250 °C for both samples (cf. inset in **Figure 1c**), with a larger loss for the as-synthesized sample (1.2 %) compared to the dried one (0.5 %), indicating a reduction of the water content in the dried sample. More structural features are revealed by the Raman spectra in **Figure 1d**, in which three distinct bands are observed, each corresponding to specific vibrational modes. First, the *F$_{2g}$* mode, associated with the in-plane bending of Sn-Cl-Sn bonds, was observed at approximately 170 cm^{-1}. The *E$_g$* mode at around

3

241 cm^{-1} is related to the asymmetric stretching of the Sn-Cl bonds.[18,19] Finally, the A_{1g} mode, corresponding to the symmetric stretching of the Sn-Cl bonds, is observed at ~ 322 cm^{-1}. The results of XPS measurements from KSC can be found in **Figure S2** in the Supporting Information. In brief, the detail spectra show in the K 2p, Sn 3d and Cl 2p regions single doublets (K 2p$_{3/2}$, Sn 3d$_{5/2}$ and Cl 2p$_{3/2}$ peaks at 294.0, 488.0 and 199.4 eV, respectively) which can be assigned to KSC.
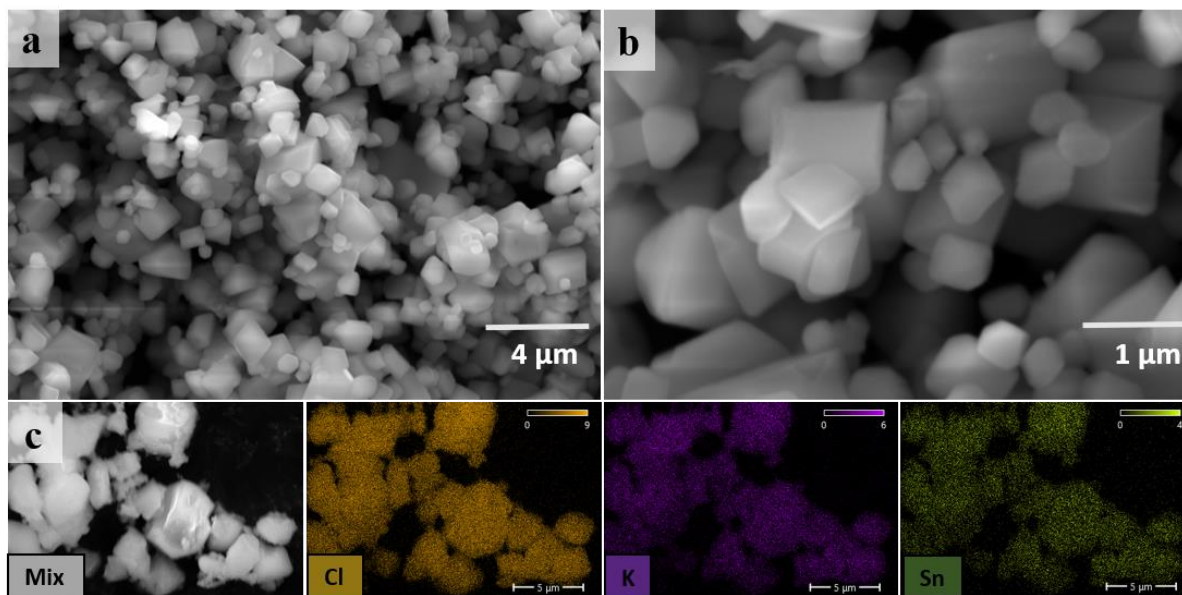

Figure 2. (a, b) FESEM images of pristine KSC and (c) EDX elemental mapping of KSC for mix, Cl, K, and Sn respectively.

Field emission scanning electron microscopy (FESEM) images were recorded to analyze the morphology and homogeneity of the KSC material. **Figure 2a, b** revealed a cube-like morphology, with individual particle sizes in the range of approximately 0.5 - 2 µm. Furthermore, energy-dispersive X-ray spectroscopy (EDX) mapping showed a homogenous distribution of the elements (Cl, K, and Sn) throughout the material. In addition, quantitative evaluation of the EDX spectrum (see **Figure S1** in the Supporting Information) corroborated the expected atomic ratio K, Sn and Cl, viz., 2:1:6 validates the composition of K_2SnCl_6 in the material studied.
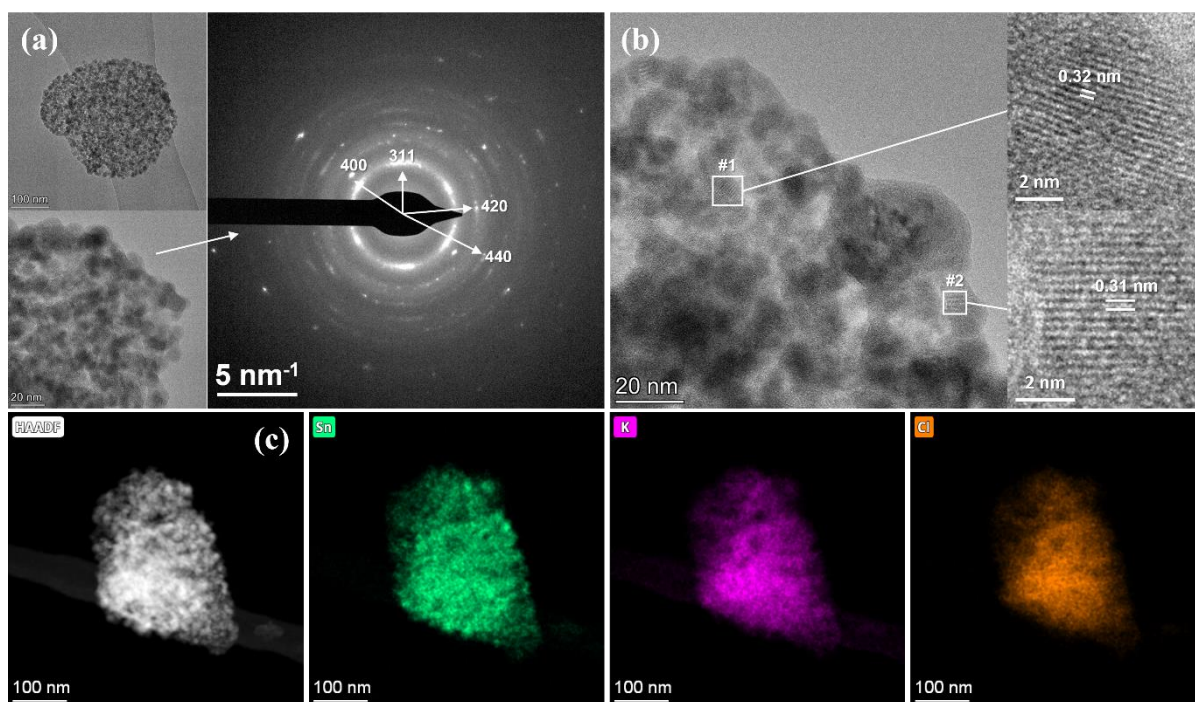
4

Figure 3. (a, b) TEM image and SAED pattern of KSC (c) high-angle annular dark-field (HAADF) and STEM-EDS elemental mapping of KSC.

The transmission electron microscopy (TEM) analysis is employed to analyze the morphology and crystal structure of KSC on a nanoscopic length scale **(Figure 3).** The selected area electron diffraction (SAED) ring pattern (**Figure 3a)** is indicative of a polycrystalline nature of the material. The SAED rings were indexed to the (311), (400), (420), and (440) crystal planes of the K_2SnCl_6 crystal structure, corresponding to d-spacings of 0.31, 0.25, 0.22, and 0.18 nm, respectively, further corroborating the XRD findings. High-resolution TEM image **(Figure 3b)** further confirms the crystalline nature of the material, with clearly visible lattice fringes. The spacing of the observed fringes was measured to be 0.31-0.32 nm, corresponding to the lattice spacing of the (311) set of planes of the K_2SnCl_6 crystal structure (ICSD collection code 1668). EDX analysis in scanning transmission electron microscopy (STEM) mode **(Figure 3c)** reveals a homogenous distribution of K, Sn, and Cl elements throughout the as-synthesized powder. The structure is polycrystalline, the composition is as expected for KSC could potentially impart the material with enhanced properties for a variety of energy storage-based applications. [20,21]

2.2. Electrochemical performance of KSC

In the next step, we come to the characterization of the electrochemical properties of KSC and its performance as an active material in a CIB. To evaluate the electrochemical performance, Swagelok cells were assembled in which KSC electrodes were coupled with metallic Li, employing 0.5 M $PP_{14}Cl$ (1-Butyl-1-methylpiperidinium chloride) in PC (propylene carbonate) as electrolyte. The cells were first investigated by cyclic voltammetry (CV) **(Figure 4a).** During the first cathodic scan of the CV, a reduction peak at approximately 0.56 V was observed, indicating a possible reduction of K_2SnCl_6 and the release of chloride ions. Subsequent cycles revealed a pair of enhanced rectangular signals at around 0.8 - 0.9 V *vs.* Li/Li$^+$ and similarly,

5

during the anodic scan, oxidation peaks were observed at 0.2 - 0.3 V *vs.* Li/Li$^+$ possibly corresponding to the reversible insertion/extraction of chloride ions into/from the electrode.
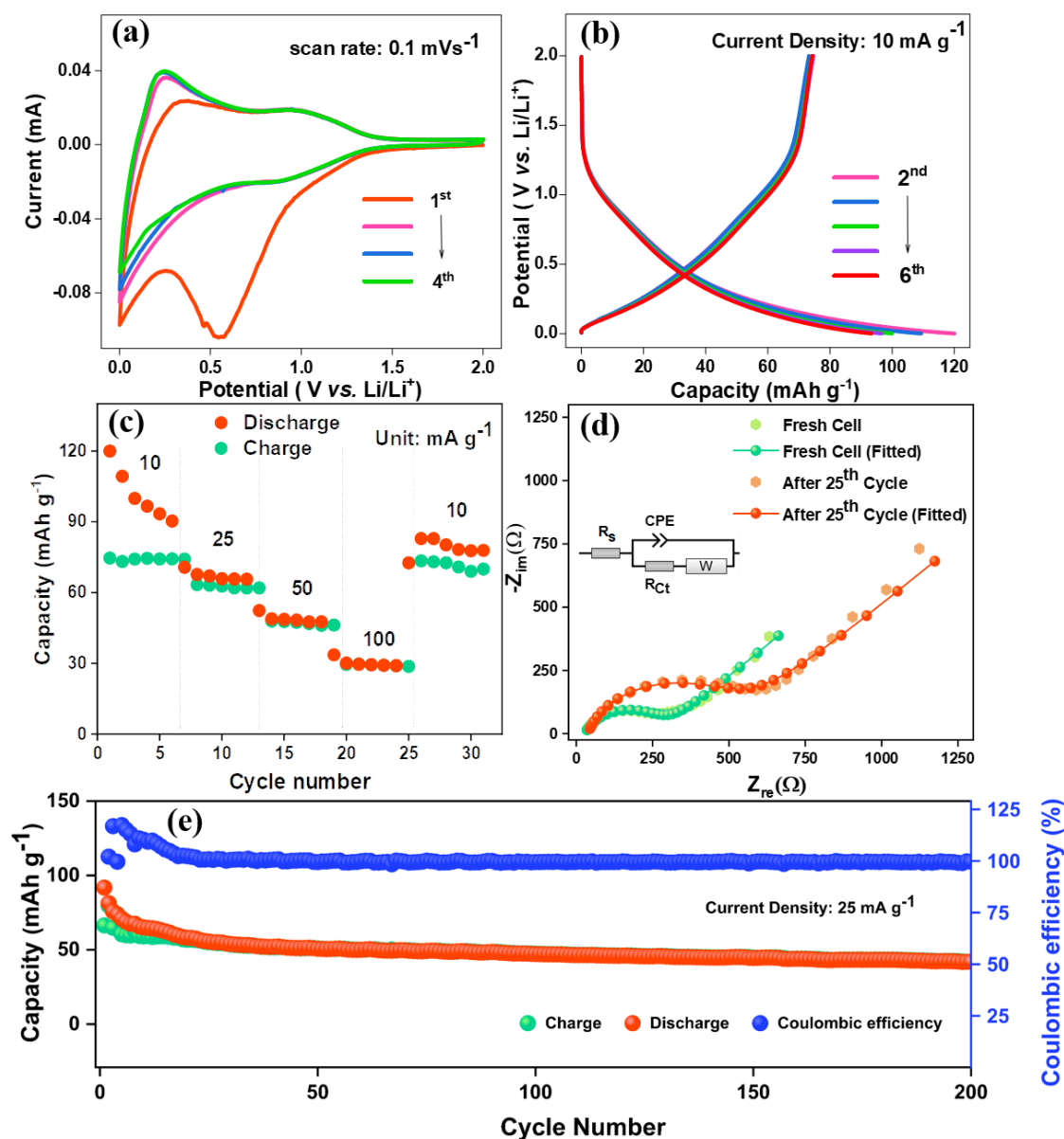

Figure 4. Electrochemical performance of KSC electrode (a) CV curve (b) charge-discharge curves (c) rate capability (d) EIS Nyquist plots with equivalent circuit model and (e) cycling stability of K_2SnCl_6/0.5M $PP_{14}Cl$/Li cell.

Further, the KSC cells were also subjected to galvanostatic cycling tests. A vast capacity loss was observed in the first cycle (**Figure S3**) at a current rate of 10 mA g^{-1}, with specific capacities of approximately 350 mA h g^{-1} in the initial discharge and only 90 mA h g^{-1} in the following charge. This result indicates the irreversible conversion of K_2SnCl_6 to tin chloride-based products, during which chloride ions are released to the lithium side. [22] The resulting conversion products act as active material in the rest of the cycling. **Figure 4b** shows the electrochemical charge-discharge profiles in the following cycles (at 10 mA g^{-1}). While the discharge capacity showed a further decay from 120 mA h g^{-1} in the second cycle to 90 mAh g$^-$

6

1 in the sixth cycle, a relatively stable charge capacity of 75 mA h g^{-1} was observed. Next, the rate capability performance of the electrode was investigated at current densities ranging from 10 to 100 mA g^{-1}, the results are shown in **Figure 4d**. With increasing current rates, the KSC electrode delivered significantly decreasing capacities. Finally, cycle life results of the KSC electrode are displayed in **Figure 4c**. A strong capacity decay was observed in the first 25 cycles (at 25 mA g^{-1}). However, after 25 cycles, the Coulombic efficiency (CE) became stable and reached ~100 %, indicating that chloride ions shuttling became more or less reversible at this point. The electrode showed a stable reversible capacity of around 51 mA h g^{-1} after 50 cycles and about 85 % of the capacity remained from the 50th to the 200th cycle. The electrochemical impedance spectroscopy (EIS) Nyquist plots **(Figure 4d)** reveal a 45° sloping line in low-frequency Warburg region, which is characteristic of a diffusion-limited charge storage process. In the medium-high frequency range, semicircles are found representing the charge transfer resistance, which is approximately 280 Ω, suggesting a strong interface connection between the electrode and the electrolyte. Nevertheless, an observed increase in charge transfer resistance after 25 cycles could be attributed to the electrode degradation on the surface due to stress induced by cycling.[23,24]

2.3 Structural and chemical evolution during electrochemical cycling
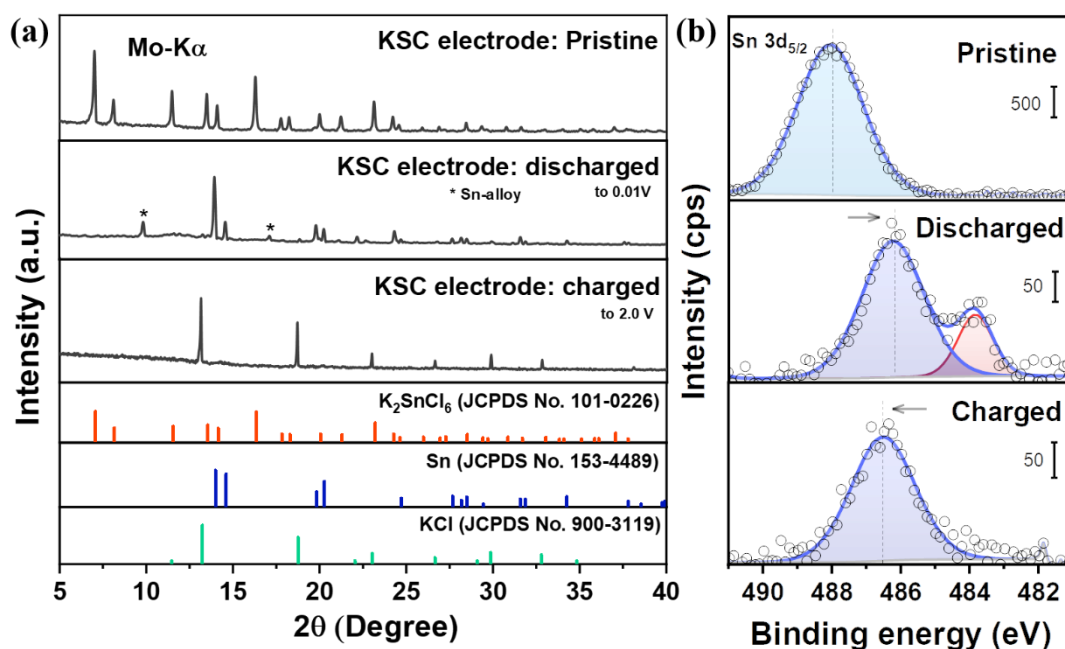

Figure 5. *Ex-situ* characterization of KSC electrodes after electrochemical cycling (a) XRD patterns of pristine, discharged and charged electrodes(b) Sn 3d$_{5/2}$ XPS detail spectra of pristine, discharged (to 0.01 V), and charged (to 2.0 V) electrodes.

The XRD patterns of the KSC electrodes **(Figure 5a)** show a strong loss of crystallinity from the pristine electrode to the first discharge, suggesting that the K$_2$SnCl$_6$ phase transforms into an amorphous phase with smaller contributions from crystalline K-Sn alloy(s), metallic Sn and KCl. In agreement with the predictions from DFT calculations, this transformation is likely associated with a conversion-type mechanism of electrode reaction, in which the Sn^{4+} ions are reduced to metallic Sn or K-Sn alloy(s), while chloride ions are released. The observed

7

amorphization of the active material is not an uncommon finding for conversion electrodes. For example, amorphization was also reported from Mössbauer spectroscopy studies for the lithiation process in $Fe_{0.5}TiOPO_4$ [25] and SnO_2[26] electrodes. Furthermore, chloride-ion cathodes such as BiOCl[8], $WOCl_4$[27] and FeOCl[28] have witnessed similar behavior. To get further information on the discharged products, complementary characterization techniques are necessary. The diffraction pattern of the charged electrode sample showed a similar amorphous pattern, but only KCl peaks were visible. This suggests that the chloride ions released during discharge were incorporated into the KCl phase and that this phase also persists upon charge. **Figure S6** of the supporting information shows the XRD pattern of the lithium metal anode after 150 cycles (discharged state). The diffraction pattern shows the formation of LiCl, which confirms that the chloride ions have shuttled from the KSC electrode to the Li side during cycling. The FESEM images in **Figure S5** depict the structural changes observed in both the KSC and Li metal electrodes after 150 cycles.

XPS was used to investigate the elemental composition and the chemical oxidation states of KSC in the pristine, fully discharged, and charged electrodes. Most importantly, **Figure 5b** compares the XPS deconvoluted spectra in the Sn $3d_{5/2}$ region. Similarly, deconvoluted spectra of the Cl 2p region are shown in **Figure S4**. For pristine KSC, a single Sn $3d_{5/2}$ peak is observed at 488.0 eV, which can be assigned to the hexachlorostannate ($SnCl_6^{2-}$) ion of KSC.[29] For the discharged electrode, the disappearance of this peak indicates complete decomposition of KSC while the detection of two new peaks at lower binding energy (Sn $3d_{5/2}$ peaks at 483.8 eV and 486.2 eV), indicates that at least partial reduction of Sn.[29] In addition, the first (smaller) peak could be assigned to K-Sn alloy(s) since its binding energy is well below the expected value for metallic Sn (of ~ 485 eV)[29] and the second one could be due to the formation of $SnCl_2$ or $KSnCl_3$,[29] which is consistent with the DFT findings, involvement of other Sn^{2+}/Sn^{4+} species cannot be excluded, however, since the binding energies of compounds with these two oxidation states are usually close to each other. After the charged state, only one peak remains, which is shifted to 486.5 eV. This shift could point to an increase in the average Sn oxidation state, i.e., the presence of a larger amount of Sn^{4+} species. In any case, the reformation of KSC can be excluded based on this result.[29]

2.4 DFT Investigations

The previous section indicated a loss of crystallinity of KSC during discharge which could not be reversed after charging indicating a decomposition of pristine KSC in the first cycle. In order to shed light on this decomposition we have performed periodic density functional theory calculations. For the computational details, we refer to the experimental section. As a potential degradation mechanism, we considered reactions of the type $K_2SnCl_6 + Li \rightarrow K_2SnCl_x + LiCl_{6-x}$ where K_2SnCl_x is the reduced KSC species with the preserved crystal structure.

To create potential K_2SnCl_x configurations, chlorine vacancies were introduced in the unit cell of pristine KSC. The cell contains n = 24 chlorine atoms. Introducing k vacancies is thus possible in $\binom{n}{k} = \left(\frac{n!}{k!(n-k)!}\right)$ different ways. This number of possible combinations is very high, but comparing the resulting geometries and removing the symmetrically equivalent ones

results in an acceptable number of structures for k = 0, 1, 2, 3, 4 **(Figure S7a)** i.e. in total 156 input structures corresponding to the stoichiometry K_2SnCl_x with $5 \leq x \leq 6$.

A DFT geometry optimization with the PBEsol functional was conducted on these input structures and the formation energies for the one-dimensional chemical space K_2SnCl_x ($5 \leq x \leq 6$) are shown in **Figure S7b**. Note that the termination at x = 5 is rather arbitrary. The plot suggests phase-separating behavior between the phases at x = 5 and the pristine phase at x = 6. These theoretical results were confirmed by geometry optimizations with the advanced SCAN functional on a set of 24 vacancy structures, which had turned out to be energetically most favorable in the previously conducted PBEsol calculations **(Figure S7b).**

Figure 6a displays the most stable structures resulting from the SCAN geometry optimization for $5 \leq x < 6$. The characteristic $SnCl_6$ octahedra becomes partly reduced upon the introduction of the vacancies but keeps their overall structure during the geometry optimization, i.e., no decomposition of the initial structure results.

To analyze the chemical stability of KSC we derived possible decomposition products as described in the experimental section. In **Figure 6b,** their stability is plotted as a function of the Cl chemical potential. Above $\varphi = 2.52\ V\ vs\ Li/Li^+$ K_2SnCl_6 is the stable compound. Upon lowering the potential, K_2SnCl_6 decomposes into $KCl + KSnCl_3$ but not into any other K_2SnCl_x compounds with $5 \leq x < 6$ since the latter are higher in energy at the relevant potential. This conversion reaction also determines the theoretical open circuit voltage (OCV) of the electrochemical system KSC/LiCl. As the potential is further lowered, at $\varphi = 2.13\ V\ vs\ Li/Li^+$ the decomposition products become $2KCl + Sn$ and eventually $\frac{42}{23}KCl + \frac{1}{23}K_4Sn_{23}$ and $KCl + KSn$ at $\varphi = 0.74\ V$ and $\varphi = 0.34\ V$, respectively. At such low potentials the energetic difference of K_2SnCl_x to its decomposition products is rather large (several 100 meV/atom) rendering the decomposition of K_2SnCl_x as an unambiguous theoretical finding.

As we determined the theoretical OCV to $2.52\ V$ and there was no electrochemical activation observed in that voltage range we conclude in agreement with section 2.3. that there is no reformation of KSC during cycling. The calculations further support the experimental finding of the formation of KCl, Sn, and K-Sn alloys as decomposition products. It is rather difficult to deduce which reactions exactly take place during cycling, but in the electrochemically active voltage range (roughly up to $1\ V$) only two possible reactions were found in the DFT calculations:

$$2KCl + Sn \xrightleftharpoons{\varphi = 0.74\ V} \frac{42}{23}KCl + \frac{1}{23}K_4Sn_{23} \xrightleftharpoons{\varphi = 0.34\ V} KCl + KSn.$$
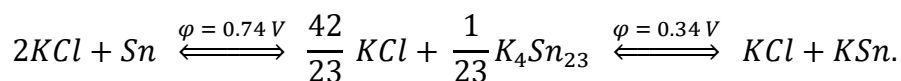
Note again that in the presented grand canonical picture, we consider a Cl reservoir represented by the LiCl anode which accounts for the stoichiometrically missing Cl in the chemical equation. Furthermore, due to the mentioned inaccuracies of the above-presented convex hull analysis, it might well be possible that in addition to the just presented reactions some other species like $SnCl_2$ or different K-Sn alloys may be involved in the reactions taking place during cycling.
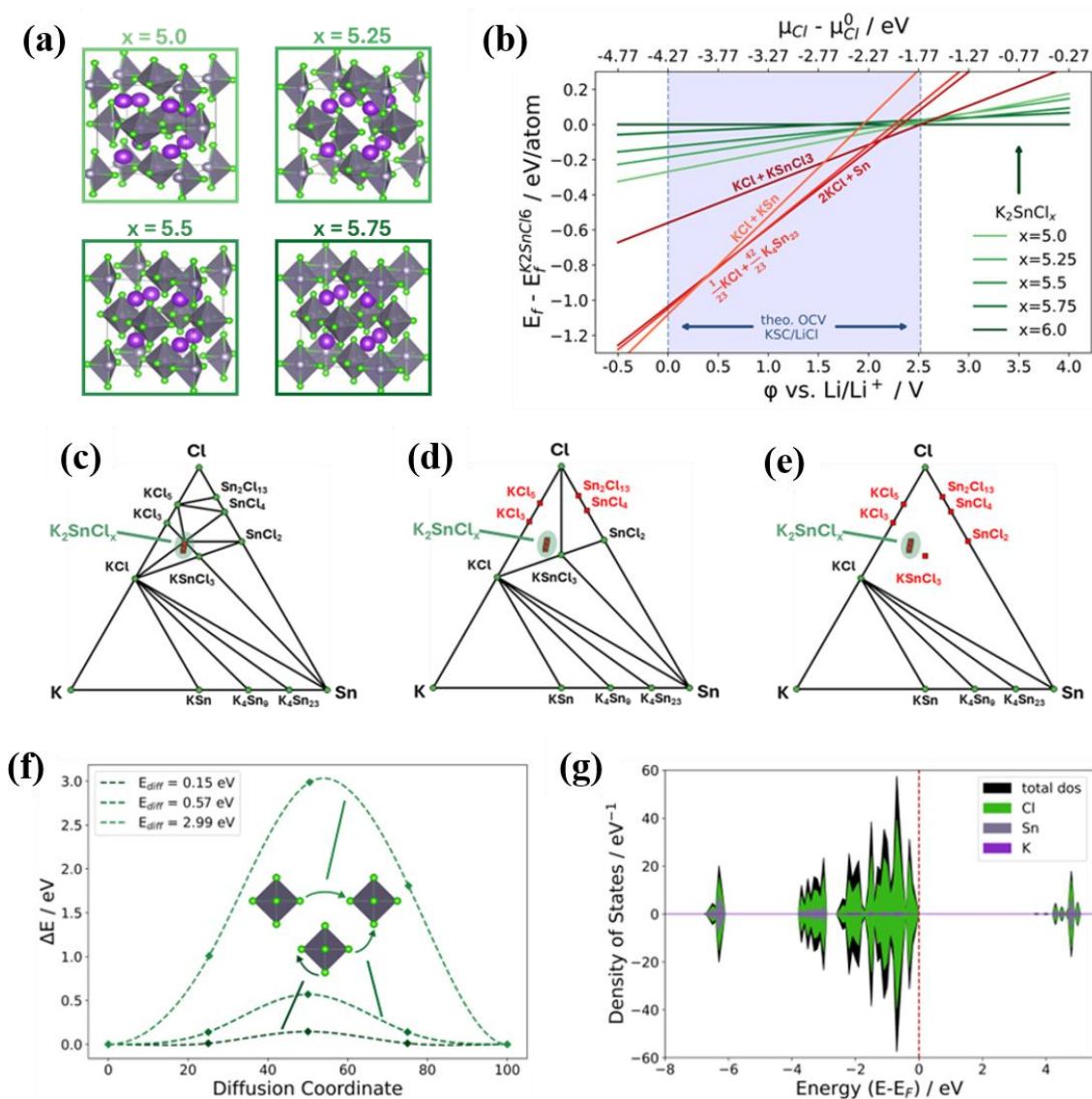
9

Figure 6. (a) Crystal structure of reduced KSC (b) Grand canonical phase diagram of K_2SnCl_x and its decomposition products (c-e) K-Sn-Cl ternary phase diagrams at $\varphi = 4.27$ V, $\varphi = 2.52$ V, and $\varphi = 1$ V vs. Li/Li$^+$ where green/red datapoints represent $E_{hull}=0$/$E_{hull}>0$ (f) Diffusion barriers and (g) density of states for pristine KSC.

In order to analyze the potentially stable structures in more detail as a function of the electrode potential, ternary phase diagrams [30,31] are displayed in **Figures 6c-e** where green and red data points represent $E_{hull} = 0$ and $E_{hull} > 0$, respectively. Of the highlighted data points in **Figure 6c** corresponding to K_2SnCl_x only K_2SnCl_6 is determined to be stable whereas the reduced compounds ($5 \leq x < 6$) display E_{hull} values somewhat larger than 0 meV/atom.

Figure 6d depicts the phase diagram at $\varphi = 2.52\,V\,vs\,Li/Li^+$ which corresponds to the theoretical decomposition potential of K_2SnCl_6. Hence, K_2SnCl_6 starts to become unstable compared to the phase diagram in Figure 6c. If, now, any of the K_2SnCl_x ($5 \leq x < 6$) compositions, which we analyzed above, corresponded to the reduced cathode material or in other words, if the electrochemical reaction during discharge was $K_2SnCl_6 + Li \rightarrow K_2SnCl_x + LiCl_{6-x}$ as hypothesized above, we would see the corresponding material being stable in the

10

phase diagram in **Figure 6d**. This is not the case. Instead, the phase diagram predicts a decomposition of K_2SnCl_6 into $KSnCl_3$ and KCl, the missing two Cl being taken by the Li electrode. Lowering the potential even further results in the phase diagram in **Figure 6e** which corresponds to $\varphi = 1\ V\ vs\ Li/Li^+$. At this potential, the phase diagram predicts KCl and Sn as decomposition products. Therefore, in line with the experimental observations discussed above the DFT calculations indicate a decomposition of K_2SnCl_6 during discharge.

3. Conclusion

In conclusion, KSC was successfully synthesized using mechanochemistry with a cubic space group *(Fm-3m).* Comprehensive structural and morphological characterization provided deeper understanding of the material's properties. Electrochemical studies were conducted to assess the potential of KSC as an electrode material for CIBs using a non-aqueous 0.5M $PP_{14}Cl$ in PC electrolyte. It demonstrated an initial discharge capacity of 350 mA h g^{-1}, but this dropped significantly to a reversible capacity of 51 mAh g^{-1} after 50 cycles at 25 mA g^{-1}. *Ex-situ* characterization techniques like XRD, XPS, and FE-SEM revealed that the electrochemical storage mechanism relies on a conversion reaction involving multiple products and the movement of chloride ions between the electrodes. Density functional theory calculations further supported the identification of these potential degradation products, which were also confirmed by experimental results. These degradation processes limit the performance of KSC as a promising electrode material for non-aqueous CIBs. This work serves as a stepping stone, inspiring future investigations into similar materials, optimization strategies, and novel electrode architectures to enhance energy storage performance in battery applications.

4. Experimental Section/ Methods

Reagents and Materials
Potassium chloride (KCl, 99 %) and tin chloride pentahydrate ($SnCl_4 \cdot 5H_2O$, 98 + % analytical grade) were purchased from Sigma-Aldrich. Super P was carbon procured from Thermo Fisher Scientific. All reagents were used directly without further purification.

Synthesis of K_2SnCl_6
A stoichiometric mixture of potassium chloride (KCl) and tin chloride pentahydrate ($SnCl_4.5H_2O$) was ball milled for 12 h, at 400 rpm using a planetary ball mill with a ball-to-material weight ratio of 20:1. The filling and emptying of the grinding jars took place in a glovebox with a dry Ar environment to prevent any contact with O_2 or moisture. The milled powder was then dried at 150 °C for 4 h in a vacuum oven to remove the residual moisture. This dried sample is used as an active material for the electrode.

Preparation of Electrodes
The KSC electrodes were fabricated according to the following procedure: The active material, conductive carbon was mixed at a weight ratio of 8:2 by grinding for 30 min in a mortar and pasted in a Mo current collector. The average mass loading was around ~ 1.2 mg cm^{-2}.

Electrochemical Measurements

The electrochemical measurements were performed with Swagelok cells that were assembled inside a glove box, using a Biologic VMP3 electrochemical workstation. KSC and Li foil (MTI corporation) were used as working and counter electrodes, respectively, and a glass fiber sheet (Whatman) was inserted as a separator. 0.5 M $PP_{14}Cl$ (1-Butyl-1-methylpiperidinium chloride) in PC was used as a non-aqueous electrolyte. The cyclic voltammetry (CV) tests were carried out with a scan rate of 0.2 mV s^{-1} in the voltage window of 0.01 to 2.0 V. The galvanostatic charge-discharge and rate capability tests of the system were carried out at room temperature in the voltage range from 0.01 to 2 V. The cells were allowed to rest for 6 hours before operations. The specific capacity of each cell was calculated based on the mass of the active material.

Material Characterization

The crystal structure and phase purity of electrodes were analysed using X-ray powder diffraction (XRD, *Stoe* STADI P XRD diffractometer) in Debye-Scherrer geometry using a Mo Kα X-ray source (λ = 0.0709 nm) at 50 kV, 40 mA. Diffraction patterns were recorded in a 2θ angle range between 5 and 40°.

The micromorphology and composition of the as-prepared samples were investigated by a scanning electron microscope (SEM, ThermoFisher Scientific Apreo 2 SEM) at an accelerating voltage of 20 kV. In addition, energy-dispersive X-ray spectroscopy (EDX) was used for elemental mapping.

Transmission electron microscopy (TEM) was conducted using a Talos F200i microscope (Thermo Fisher Scientific) operating at an accelerating voltage of 200 kV using Velox software. The high-angle annular dark-field (HAADF) imaging and the EDX analysis were performed in STEM mode using Dual Bruker XFlash 6-100 EDS Detectors. For TEM sample preparation, KSC power was dried at 80 °C in an oven overnight. Then, the carbon-coated Formvar film of a copper TEM grid was gently rubbed on the fine powders.

An inVia confocal Raman microscope (RENISHAW) with a 532 nm laser as an excitation light source was used to collect Raman spectra. The samples were illuminated by focusing the laser light through a 50× objective (Carl Zeiss). The spectral range was set to 50–400 cm^{-1} with a spectrum acquisition time of 2 seconds.

TGA measurements were performed with a NETZSCH TG 209F1 Libra. The sample material was loaded into an alumina crucible. The measurement range was from 30°C to 600°C at a rate of 10°C/min.

X-ray photoelectron spectroscopy (XPS) measurements were carried out with a PHI 5800 MultiTechnique ESCA System. To avoid surface contamination, the samples were transferred after preparation in a glove box in an inert gas atmosphere to the sample load lock of the XPS system. The spectra were recorded using monochromatized Al Kα radiation (300 W, 15 kV) and pass energies at the analyzer of 93.9 and 29.35 eV for survey and detail spectra, respectively. Sample charging effects were relatively small; hence, neutralization was not necessary. All binding energies were calibrated to the C1s peak of adventitious carbon at 284.8 eV. The peak fit of the XPS results was done with CasaXPS, using Shirley-type backgrounds and Gaussian-Lorentzian peak shapes. For the peak fit of the Cl 2p, K 2p and Sn 3d peak doublets, the expected intensity ratios and spin-orbit splits were inserted. [29]

DFT calculations

The KSC unit cell contains 36 atoms and was used for all DFT calculations. As the widely used exchange-correlation functional suggested by Perdew, Burke, and Ernzerhof [32] results in a lattice constant of 10.25 Å which is far above the experimental value of 10.01 Å, in addition, the PBEsol [33] functional and the SCAN [34] functional were tested. The resulting values for the lattice constant, 9.97 Å and 9.96 Å respectively, agree far better with the experimental result. Consequently, the PBEsol functional was used for most of the geometry optimizations and the more computationally expensive SCAN meta-generalized gradient approximation, which is known to yield significantly improved formation energies compared to generalized gradient approximation-based functionals,[35] was used for certain samples only. The density of states was determined by employing the HSE06 functional.[36] The ionic cores were treated with the projector augmented wave method,[37] as implemented in the Vienna Ab Initio Simulation Package.[38–40] Electronic wave functions were expanded up to energies of 600 eV and it was made sure that total energies converged within a few meV/atom concerning the number of k-points in the first Brillouin zone. All structures were optimized until the entries of the stress tensor and all forces were below 0.01 eV/Å without constraining any internal degree of freedom.

The chemical stability of the system at hand was analysed based on the concept of the energy above hull E_{hull}. This entity describes the energetic difference of a certain atomic configuration (i.e. a material) to the energetically most favourable configuration with the same stoichiometry and is thus a computational measure for thermodynamic stability.[41] $E_{hull} = 0$ eV corresponds to a thermodynamically stable compound whereas $E_{hull} > 0$ eV indicates instability. Still, due to inaccuracies of DFT and metastability, one must take these numbers with caution.[41] Often compounds are found to be stable for values of E_{hull} up to about 100 meV/atom.[42] Potential allotropes and decomposition products were taken from a database of roughly 115000 compounds, which comprises the convex hull (i.e. all compounds with $E_{hull} = 0$ eV) of the entire chemical space.[43,44] More details on the calculational procedure can be found in a previous publication, the only difference being the underlying database.[45]

Note that the determination of the stability requires the choice of the appropriate reference system. Typically, the reference point for the chemical potential of chlorine μ_{Cl} at standard conditions is gaseous Cl_2. However, in a chloride ion battery the appropriate reference is given by the LiCl formation at the anode side which becomes further modified by the electrode potential φ of the battery. Effectively, the chemical potential of chlorine is given by [46] $\mu_{Cl} = \mu_{Cl}^{LiCl} + e\varphi$, where μ_{Cl}^{LiCl} is the chemical potential of chlorine in LiCl which is shifted by 4.27 eV concerning the chlorine chemical potential of Cl_2 at standard conditions μ_{Cl}^0, e is the elemental charge and φ is the electrode potential in $V\ vs\ Li/Li^+$.

The barriers for Cl⁻ diffusion were investigated via the nudged elastic band (NEB) method.[47] We investigated three different diffusion paths in the low vacancy limit where each path was modelled with three distinct intermediate images. Optimized NEB algorithms were used to optimize the ion positions until the forces on every ion were lower than 0.05 eV/Å.[48] The climbing image method was used to ensure that the transition state was found.[49]

13

Data availability statement

All electronic structure calculations used in this work are made available under the Creative Commons Attribution license (CC BY 4.0) on the NOMAD repository (https://nomad-lab.eu) within the dataset "KSC_as_Cl_ion_battery_cathode", https://dx.doi.org/10.17172/NOMAD/2024.07.15-1.

Acknowledgments

References

[1]   J.-M. Tarascon, M. Armand, *Nature* **2001**, 359.

[2]   J. Biemolt, P. Jungbacker, T. van Teijlingen, N. Yan, G. Rothenberg, *Beyond lithium-based batteries*, Vol. 13, MDPI AG, **2020**.

[3]   I. D. Hosein, *ACS Energy Lett* **2021**, *6*, 1560.

[4]   G. Karkera, M. A. Reddy, M. Fichtner, *J Power Sources* **2021**, *481*.

[5]   F. Gschwind, H. Euchner, G. Rodriguez-Garcia, *Chloride Ion Battery Review: Theoretical Calculations, State of the Art, Safety, Toxicity, and an Outlook towards Future Developments*, Vol. 2017, Wiley-VCH Verlag, **2017**, pp. 2784–2799.

[6]   G. Karkera, M. A. Reddy, M. Fichtner, *J Power Sources* **2021**, *481*.

[7]   C. Zhang, *Nat Energy* **2016**, *1*.

[8]   X. Zhao, Z. Zhao-Karger, D. Wang, M. Fichtner, *Angewandte Chemie - International Edition* **2013**, *52*, 13621.

[9]   X. Hu, F. Chen, S. Wang, Q. Ru, B. Chu, C. Wei, Y. Shi, Z. Ye, Y. Chu, X. Hou, L. Sun, *ACS Appl Mater Interfaces* **2019**, *11*, 9144.

[10]   K. P. Lakshmi, K. J. Janas, M. M. Shaijumon, *J Power Sources* **2019**, *433*.

[11]   Y. Cao, J. Liang, X. Li, L. Yue, Q. Liu, S. Lu, A. M. Asiri, J. Hu, Y. Luo, X. Sun, *Recent advances in perovskite oxides as electrode materials for supercapacitors*, Vol. 57, Royal Society of Chemistry, **2021**, pp. 2343–2355.

[12]   T. Xia, Y. Li, L. Huang, W. Ji, M. Yang, X. Zhao, *ACS Applied Materials & Interfaces* **2020**, *12*, 18634.

[13]   G. Karkera, M. Soans, A. Akbaş, R. Witter, H. Euchner, T. Diemant, M. A. Cambaz, Z. Meng, B. Dasari, S. G. Chandrappa, P. W. Menezes, M. Fichtner, *Adv Energy Mater* **2023**.

[14]   J. F. Ackerman, *Mat. Res. Bull* **1984**, *19*, 783.

[15]   H. Zhang, L. Zhu, J. Cheng, L. Chen, C. Liu, S. Yuan, *Crystals (Basel)* **2019**, *9*.

[16]   R. G. Dickinson, *J Am Chem Soc* **1922**, *44 (2)*.

[17]   J. A. Lerbscher, J. Trotter, *Notes for Authors, Acta Cryst* **1976**, *32*, 2671.

[18]   Y. Morioka, I. Nakagawa, *JOURNAL OF RAMAN SPECTROSCOPY* **1987**, *18*, 533.

[19]   J. Pelzl, P. Enuels, I. Florian, *phys. stat. sol. (b)* **1977**, *82*.

[20]   A. Bekhti Siad, M. Baira, M. B. Siad, *Journal of Physics and Chemistry of Solids* **2021**, *152*.

[21]   M. M. Byranvand, W. Zuo, R. Imani, M. Pazoki, M. Saliba, *Tin-based halide perovskite materials: properties and applications*, Vol. 13, Royal Society of Chemistry, **2022**, pp. 6766–6781.

[22]   P. Gao, M. A. Reddy, X. Mu, T. Diemant, L. Zhang, Z. Zhao-Karger, V. S. K. Chakravadhanula, O. Clemens, R. J. Behm, M. Fichtner, *Angewandte Chemie* **2016**, *128*, 4357.

[23]   Y. Abe, N. Hori, S. Kumagai, *Energies (Basel)* **2019**, *12*.

[24]   P. Mudgal, H. Arora, J. Pati, M. K. Singh, M. Khetri, R. S. Dhaka, *Proceedings of the Indian National Science Academy* **2022**, *88*, 430.

[25]   P. Bleith, H. Kaiser, P. Novák, C. Villevieille, *Electrochim Acta* **2015**, *176*, 18.

[26]   Z. Huang, H. Gao, Z. Yang, W. Jiang, Q. Wang, S. Wang, J. Ju, Y. U. Kwon, Y. Zhao, *Mater Des* **2019**, *180*.

[27]   G. Karkera, M. Soans, B. Dasari, E. Umeshbabu, M. A. Cambaz, Z. Meng, T. Diemant, M. Fichtner, *Energy Technology* **2022**, *10*.

[28]   X. Zhao, Q. Li, T. Yu, M. Yang, K. Fink, X. Shen, *Sci Rep* **2016**, *6*.

[29]   J. F. Moulder, W. F. Stickle, P. E. Sobol, K. D. Bomben, J. Chastain, *Handbook of X-ray Photoelectron Spectroscopy, Perkin Elmer Corp.*, **1992**.

[30]   S. P. Ong, L. Wang, B. Kang, G. Ceder, *Chemistry of Materials* **2008**, *20*, 1798.

[31]   S. P. Ong, A. Jain, G. Hautier, B. Kang, G. Ceder, *Electrochem commun* **2010**, *12*, 427.

[32]   J. P. Perdew, K. Burke, M. Ernzerhof, *Generalized Gradient Approximation Made Simple*, **1996**.

[33]   J. P. Perdew, A. Ruzsinszky, G. I. Csonka, O. A. Vydrov, G. E. Scuseria, L. A. Constantin, X. Zhou, K. Burke, *Phys Rev Lett* **2008**, *100*.

[34]   J. Sun, A. Ruzsinszky, J. Perdew, *Phys Rev Lett* **2015**, *115*.

[35]   Y. Zhang, D. A. Kitchaev, J. Yang, T. Chen, S. T. Dacek, R. A. Sarmiento-Pérez, M. A. L. Marques, H. Peng, G. Ceder, J. P. Perdew, J. Sun, *NPJ Comput Mater* **2018**, *4*.

[36]   A. V. Krukau, O. A. Vydrov, A. F. Izmaylov, G. E. Scuseria, *Journal of Chemical Physics* **2006**, *125*.

[37]   P. E. Blochl, *PHYSICAL REVIEW B* **1994**, *50*, 17953.

[38]   G. Kresse, D. Joubert, *Phys Rev B* **1999**, *59*, 1758.

[39]   G. Kresse, J. Furthmü, *Phys Rev B* **1996**, *54*, 11169.

[40]   G. Kresse, J. Hafner, *Phys Rev B* **1993**, *47*, 558.

[41]   C. J. Bartel, *Review of computational approaches to predict the thermodynamic stability of inorganic solids*, Vol. 57, Springer, **2022**, pp. 10475–10498.

[42]   W. Sun, S. T. Dacek, S. P. Ong, G. Hautier, A. Jain, W. D. Richards, A. C. Gamst, K. A. Persson, G. Ceder, *Sci Adv* **2016**, *2*.

[43]   J. Schmidt, L. Pettersson, C. Verdozzi, S. Botti, M. A. L. Marques, *Sci. Adv* **2021**, *7*, 7948.

[44]   J. Schmidt, N. Hoffmann, H. C. Wang, P. Borlido, P. J. M. A. Carriço, T. F. T. Cerqueira, S. Botti, M. A. L. Marques, *Advanced Materials* **2023**, *35*.

[45]   J. Döhn, A. Groß, *Advanced Energy and Sustainability Research* **2024**, *5*.

[46]   H. Euchner, A. Groß, *Phys Rev Mater* **2022**, *6*.

[47]   G. Henkelman, H. Jónsson, *Journal of Chemical Physics* **1999**, *111*, 7010.

[48]   D. Sheppard, R. Terrell, G. Henkelman, *Journal of Chemical Physics* **2008**, *128*.

[49]   G. Henkelman, B. P. Uberuaga, H. Jónsson, *Journal of Chemical Physics* **2000**, *113*, 9901.

16